



Bifunctional core-shell architecture allows stable H₂ production utilizing CH₄ and CO₂ in a catalytic chemical looping process

Davood Hosseini, Paula M. Abdala, Felix Donat, Sung Min Kim, Christoph R. Müller*

Laboratory of Energy Science and Engineering, Department of Mechanical and Process Engineering, ETH Zurich, Leonhardstrasse 21, 8092, Zürich, Switzerland

ARTICLE INFO

Keywords:

Dry reforming of methane
Hydrogen
Bifunctional
Core-shell
Chemical looping

ABSTRACT

We report on the development of a bifunctional catalyst (Pt) - oxygen carrier (Fe₂O₃) that integrates the dry reforming of methane (DRM) into the chemical looping-based production of hydrogen. The material exhibits a high and stable methane conversion (~80%) and hydrogen yield (10.8 mmol/g catalyst-oxygen carrier) with only a small quantity of impurities (CO, CO₂ < 2 ppm). The structural changes of the material are followed by operando X-ray powder diffraction and X-ray absorption spectroscopy coupled with gas chromatography. Insight into the evolution of the size of the Pt nanoparticles and their interaction with CeO₂ are probed by transmission electron microscopy and X-ray absorption fine structure analysis. Under DRM conditions, the Pt nanoparticles grow in size, however, their re-dispersion on the CeO₂ support (via PtO_x-support interaction) during air oxidation recovers their activity in the consecutive cycle.

1. Introduction

Hydrogen (H₂) is a clean energy carrier that can play a significant role in reducing greenhouse gas emissions. However, within a sustainable energy landscape, H₂ must be produced in a sustainable manner without the additional emissions of greenhouse gases. Currently, on the large scale, H₂ is produced predominantly via the steam methane reforming (SMR) or the gasification of coal resulting in significant CO₂ emissions. [1] In such schemes, additional, energy-intensive purification steps are required to yield H₂ of high purity that satisfies the requirements of polymer electrolyte membrane fuel cells (PEMFC) to prevent poisoning of the Pt electrodes. [2] An alternative process to produce pure H₂ directly from carbonaceous fuels is the chemical looping-based H₂ production (CLH), also referred to as chemical looping water splitting, relying typically on an iron-based oxygen carrier. Different from the conventional SMR process, the H₂ produced via CLH does not require further purification steps, while it is similarly efficient from an exergetic point of view as SMR. [3,4]

The CLH is a cyclic, three-step process that involves the redox reactions of a solid oxygen carrier material (typically iron oxide) to produce H₂ free of CO_x from steam. In the first step, a gaseous fuel reduces the Fe₂O₃-based oxygen carrier. In the second step, the reduced oxygen carrier is re-oxidized with steam (3Fe + 4H₂O → Fe₃O₄ + 4H₂) yielding high-purity H₂, after the condensation of unconverted steam. The third step is to fully oxidize back the reduced oxygen carrier to its

original state (*i.e.* Fe₂O₃). The third step is also highly exothermic, yielding a significant amount of heat suitable for heat integration. A key feature of the chemical looping process is that the oxygen required to oxidize the fuel in the reduction step is transferred from air and steam via the solid oxygen carrier. Therefore, the reducing gases or the gaseous products of the reduction step (CO₂, CO, H₂O) are never in contact with the steam/H₂ stream, thus avoiding expensive gas separation for purification of the H₂ produced.

In a chemical looping process, the reduction of the oxygen carrier is usually performed by CO or a synthesis gas (a mixture of CO and H₂) derived via the gasification of coal or biomass. Since CO and synthesis gas are not primary fuels, their use imposes further costs to the process. On the other hand, the use of natural gas, an abundant primary fuel containing mainly CH₄, has great potential to make the process economically more attractive. [5,6] However, there are two main challenges associated with using CH₄ in the reduction step: (i) a poor reactivity of Fe₂O₃ with CH₄, resulting in a low degree of reduction and hence a low yield of H₂ and (ii) at the high operating temperatures (700–1000 °C) thermal decomposition of CH₄ (CH₄ → C + 2H₂) occurs, which causes coke deposition on the oxygen carrier and thus contaminates the H₂ produced during steam oxidation with CO. Therefore, the development of strategies to enable the utilization of CH₄ in the CLH process are highly relevant.

An attractive solution to overcome the aforementioned problems associated with the use of CH₄ is the coupling of the dry reforming of

* Corresponding author.

E-mail address: muelchri@ethz.ch (C.R. Müller).

<https://doi.org/10.1016/j.apcatb.2019.117946>

Received 21 May 2019; Received in revised form 8 July 2019; Accepted 9 July 2019

Available online 13 July 2019

0926-3373/ © 2019 Elsevier B.V. All rights reserved.

methane (DRM) reaction with the CLH process, which is also referred to as catalyst-assisted chemical looping dry reforming. [7] In the DRM reaction two major greenhouse gases (viz. CO_2 and CH_4) are catalytically converted into a synthesis gas ($\text{CH}_4 + \text{CO}_2 \rightarrow 2\text{H}_2 + 2\text{CO}$). In the coupled process, the oxygen carrier is reduced *in situ* by the synthesis gas produced during DRM and is oxidized in a second step by CO_2 or H_2O to yield CO or H_2 , respectively. The coupled process requires a reactor bed composed of i) a highly active DRM catalyst and ii) an oxygen carrier that is stable over multiple (catalytic) redox cycles, either as a physical mixture or integrated into a bifunctional material.

The coupling of DRM and CLH to produce CO_x -free H_2 , allowing the utilization of CH_4 in the reduction step, has been demonstrated using a physical mixture of a $\text{Ni-Al}_2\text{O}_3$ catalyst and iron oxide as the oxygen carrier. [8] However, a considerable decrease in the H_2 yield was observed over the first ten cycles with a drop of 30% compared to the quantity of hydrogen produced in the first cycle (from ~4.9 to 3.6 mol $\text{H}_2/\text{kg Fe}_2\text{O}_3$). Moreover, coke deposits on the surface of the Ni-based catalyst led to the contamination of H_2 by CO (100–200 ppm), which was released during the steam oxidation step due to their gasification. Further material development is needed to overcome these drawbacks.

More recently, attention has been directed towards the advancing of bifunctional materials that contain a catalyst and an oxygen carrier. Most of the recent developments have focused on integrating DRM into the chemical looping-based conversion of CO_2 to CO , where the reduced material is oxidized by CO_2 instead of steam ($3\text{Fe} + 4\text{CO}_2 \rightarrow \text{Fe}_3\text{O}_4 + 4\text{CO}$). [7,9] For this reaction scheme, a material containing 5 wt.% Ni on Fe_2O_3 - CeO_2 (1:1) has been reported. Here, Ni acts as the DRM catalyst to produce a synthesis gas that reduces iron oxide. [7] During reduction, the accumulation of carbon was observed. However, these carbon species were removed during CO_2 oxidation. Despite the promising results obtained for the production of CO from CO_2 , the development of bifunctional materials that allow for the coupling of DRM and CLH has not been reported yet. One of the main drawbacks of formulations that contain Ni-based DRM catalysts is the formation of coke that would lead to the production of CO during steam oxidation, resulting in a contamination of the H_2 produced. In contrast, noble metals such as Pt, Ru and Rh exhibit a high activity for DRM and are fairly resistant to carbon deposition, but show some tendency for sintering. [10–12] Due to the relatively high cost of these noble metals, minimizing their loading and controlling their dispersion is important. In this context, the type of support plays a key role. For instance, CeO_2 based supports have been reported to prevent deactivation by sintering. [13,14] The re-dispersion of Pt on CeO_2 by treatment under oxidative conditions at high temperature (via Pt-oxide-support interaction) has been proposed as a key feature in the minimization of sintering. [15–17] The fact that a catalyst can be “regenerated” under oxidative conditions would be advantageous also in the DRM-chemical looping.

Herein, we report the design of a bifunctional (catalyst-oxygen carrier) $\text{Fe}_2\text{O}_3@/\text{CeO}_2$ -Pt that allowed to integrate efficiently the DRM into CLH with a cyclically stable performance. The material contained a $\text{Fe}_2\text{O}_3@/\text{CeO}_2$ core-shell structure decorated with Pt nanoparticles. The Pt nanoparticles supported on CeO_2 acted as the DRM catalyst. CeO_2 was selected as the shell material to ensure a stable cyclic redox performance of the oxygen carrier (Fe_2O_3) by reducing sintering, and allowed for the re-dispersion of Pt nanoparticles under air treatment. The schematic of the material components functionality along with the reactions taking place in each step are presented in Fig. 1. The material developed exhibited high and stable DRM conversion (~80%), allowing to fully reduce the oxygen carrier in the first redox step under DRM conditions, and to produce CO_x -free (< 2 ppm) H_2 in the oxidation step by steam, with a cyclically stable yield (10.8 mmol/g catalyst-oxygen carrier), outperforming previous developments. [8]

The structural changes of the bifunctional catalyst-oxygen carrier were followed by combining *operando* synchrotron X-ray powder diffraction (XRD) and Fe K-edge X-ray absorption spectroscopy (XAS) complemented by analyses using energy dispersive spectroscopy (EDS)

coupled with scanning transmission electron microscopy (STEM). XRD, XAS (Fe K-edge) and reactivity measurements revealed that iron oxide is fully reduced to metallic Fe during DRM conditions, leading in turn to a high H_2 yield which is close to the theoretically expected value (considering reduction of Fe_2O_3 to Fe) in the subsequent water splitting step (oxidation step). Catalytic studies, in combination with TEM and Pt L_{III}-edge XAS, show that the material lost some of its DRM activity owing to sintering of the Pt nanoparticles. We also demonstrate that after oxidation in air, the Pt nanoparticles were partially oxidized and re-dispersed on the CeO_2 surfaces, recovering the initial catalytic activity in the next reaction cycle.

2. Experimental

2.1. Materials synthesis

2.1.1. Synthesis of $\text{Fe}_2\text{O}_3@/\text{CeO}_2$ core-shell structures

2.1.1.1. Synthesis of Fe_3O_4 sub-micrometer spheres. The magnetite (Fe_3O_4) particles were synthesized via a solvothermal method, [18,19] where 2.5 g of $\text{FeCl}_3 \cdot 6\text{H}_2\text{O}$, 0.6 g of trisodium citrate and 4.3 g of sodium acetate were dissolved in 80 mL of ethylene glycol under stirring for 60 min. The mixture was transferred into a teflon-lined stainless-steel autoclave (with a capacity of 200 mL). After heating the autoclave at 200 °C for 12 h, it was cooled down to room temperature. The black product was washed with deionized water and ethanol for several times, and finally dried at 50 °C for 3 h.

2.1.1.2. Synthesis of $\text{Fe}_3\text{O}_4@/\text{CeO}_2$ core-shell structures. The as-prepared Fe_3O_4 sub-micrometer spheres were coated by CeO_2 via a chemical precipitation method. [20] Typically, 0.5 g of Fe_3O_4 sub-micrometer spheres were dispersed in 100 mL deionized water and 0.75 g $\text{Ce}(\text{NO}_3)_3 \cdot 6\text{H}_2\text{O}$ was dissolved in 100 mL ethanol. After mixing the two solution using ultrasound, an aqueous solution containing 0.75 g hexamethylenetetramine (HMT) and 2 mL deionized water was added and the resultant mixture was mechanically stirred in an oil bath at 65 °C for 1 h. The products were collected by a magnet and washed with deionized water and ethanol for several times, and finally dried at 50 °C for 3 h followed by calcination at 800 °C for 2 h.

2.1.2. Synthesis of the reference Fe_2O_3 - CeO_2 material by co-precipitation

Co-precipitation was performed at pH 12 using NaOH as the precipitating base. First iron nitrate ($\text{Fe}(\text{NO}_3)_3 \cdot 9\text{H}_2\text{O}$) and cerium nitrate ($\text{Ce}(\text{NO}_3)_3 \cdot 6\text{H}_2\text{O}$) were dissolved in de-ionized water to obtain 1 M aqueous solutions of the metal cations. Appropriate amounts of iron and cerium nitrate solutions were mixed to yield the desired mass fractions in the calcined oxygen carriers, i.e. $\text{Fe}_2\text{O}_3:\text{CeO}_2 = 65:35$. Precipitation was performed by adding a 2 M NaOH solution drop-wise to the nitrate solution under vigorous stirring. The resulting slurry was aged for 2 h at room temperature. The precipitate was filtered and washed several times with reverse osmosis water (15 MΩcm at 25 °C) to remove excess nitrate and Na^+ ions. The washing was finalized once the conductivity of the filtrate was < 200 $\mu\text{S cm}^{-1}$. Subsequently, the precipitate was dried in an oven at 100 °C overnight and then calcined in a muffle furnace at 800 °C for 2 h. Finally, the calcined oxygen carrier was crushed and sieved into the size range 50–100 μm .

2.1.3. Photodeposition of Pt nanoparticles onto the $\text{Fe}_2\text{O}_3@/\text{CeO}_2$ and Fe_2O_3 - CeO_2 particles

Pt nanoparticles were synthesized and deposited onto the calcined $\text{Fe}_2\text{O}_3@/\text{CeO}_2$ and Fe_2O_3 - CeO_2 particles using a photochemical method [21]. In a typical synthesis, 50 mg of the Fe_2O_3 based particles were dispersed in 15 mL of ethanol/water (volume ratio 1:1) in a 20 mL glass vial. After 15 min of sonication, 10 mg of PVP ($M_w = 40,000$) and 30 mg of 4-benzoylbenzoic acid were added to the solution, followed by an additional 15 min of sonication. Subsequently, 0.75 mg of H_2PtCl_6

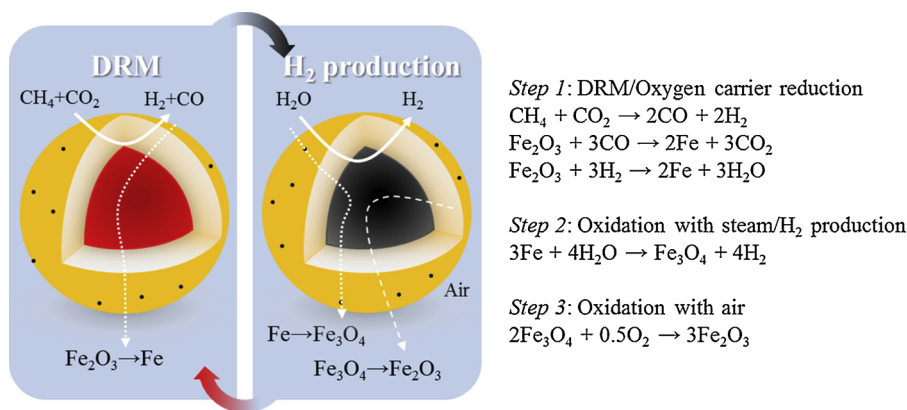


Fig. 1. Left: schematic illustration of the proposed process that integrates the DRM directly into the chemical looping H₂ production (CLH) process yielding pure H₂ using a bifunctional material. The material consists of a Fe₂O₃ core (red), coated by a CeO₂ shell (yellow) and decorated with Pt nanoparticles (black dots). Right: reactions occurring at each step are described (For interpretation of the references to colour in this figure legend, the reader is referred to the web version of this article).

was added and dissolved by magnetic stirring for 5 min. The vial was placed next to an immersion well photoreactor (RQ400, Photochemical Reactors, UK) with a distance of 5 cm. The UV treatment (200–400 nm) was conducted using a 400 W mercury lamp for 15 min. The temperature of the immersing well was kept at $23 \pm 2^\circ\text{C}$ using water cooling. The product was collected via centrifugation, washed further by water and ethanol and dried in an oven at 50°C for 3 h. The samples after Pt photodeposition are referred to as Fe₂O₃@CeO₂-Pt and Fe₂O₃-CeO₂-Pt.

2.1.4. Synthesis of the reference material CeO₂-Pt

First, CeO₂ particles were synthesized by a precipitation method. Typically, 0.75 g Ce(NO₃)₃·6H₂O was dissolved in a mixture of ethanol and water (1:1 ratio, 100 mL). After mixing the solution using ultrasound, an aqueous solution containing 0.75 g hexamethylenetetramine (HMT) and 2 mL deionized water was added and the resultant mixture was stirred in an oil bath at 65°C for 1 h. The products were collected by centrifugation and washed with deionized water and ethanol for several times, and finally dried at 50°C for 3 h followed by calcination at 800°C for 2 h. The Pt nanoparticles were deposited onto the CeO₂ particles using the photochemical method described above.

2.2. Materials characterization

A PANalytical Empyrean X-ray powder diffractometer was used for the characterization of crystalline phases of the synthesized materials. The diffractometer was equipped with a X'Celerator Scientific ultra-fast line detector and Bragg-Brentano HD incident beam optics using Cu K_α radiation (45 kV and 40 mA). The scans were collected in the 2θ range of $20^\circ - 80^\circ$ with a step size of 0.016° and scanning speed of $0.022^\circ \text{ s}^{-1}$. A diffracted beam monochromator was used to suppress unwanted fluorescence originating from iron in the samples.

High resolution scanning electron microscopy (HR-SEM) was used to morphologically characterize the calcined oxygen carriers (FEI Quanta 200 FEG microscope operated at 10 kV).

Scanning transmission electron microscopic (STEM) images and elemental maps were obtained using a FEI Talos F200X (200 kV). The microscope was equipped with a high brightness Schottky FEG and the Super-X integrated energy dispersive X-ray spectroscopy EDS system which included four silicon drift detectors (SDDs) placed symmetrically around the sample. The average Pt particle size was determined from high-angle annular dark-field scanning transmission electron microscopy (HAADF-STEM) images using the ImageJ software package. [22] The average particle size (and error bar) reported is based on the analysis of more than 100 individual particles.

Platinum quantitative analysis by inductively coupled plasma optical emission spectroscopy (ICP-OES) was carried out on an Agilent optical emission spectrometer (Agilent 5100 VDV ICP-OES). Before the ICP-OES measurement, the catalyst was digested in aqua regia for 24 h. Subsequently, deionized water was added to dilute the solution. The

sample was centrifuged prior to analysis.

Chemisorption experiments were performed in an AutoChem (Micromeritics) system. In a typical experiment, 50 mg of the as-prepared CeO₂-Pt material was reduced at 400°C for 20 min using 5 vol.% H₂ in Ar. Subsequently the sample was purged with Ar at 400°C for 20 min and cooled down to 40°C . The quantity of chemisorbed H₂ was determined at 40°C by periodically injecting pulses of 5 vol.% H₂ in Ar over the reduced material. The stoichiometry factor between dissociated H₂ and active metal (Pt) was assumed to be 1.0 (H/M).

Carbon deposition experiments were performed in a thermogravimetric analyzer (TGA, Mettler Toledo TGA/DSC). A small amount of catalyst (~50 mg) was placed in an alumina crucible and heated up to 750°C under N₂, and then exposed to DRM reaction conditions (CH₄/CO₂ (1:1) ratio, 10 vol.% balanced N₂, total flow rate: 100 mL/min). [23]

2.3. Dry reforming of methane coupled with chemical looping hydrogen production

The cycling experiments were carried out using a home-built reactor setup (Fig. S3c). The setup consisted of three main parts: (i) a gas delivery system with digital mass flow controllers (Bronkhorst) and a temperature-controlled water evaporator (Bronkhorst), (ii) a fixed-bed quartz reactor (400 mm length, 10.2 mm internal diameter) in a programmable tube furnace, and (iii) a gas analysis system using a Thermo Scientific C2V-200 micro-Gas Chromatograph (micro-GC) equipped with a thermal conductivity detector; molecular sieve 5A and U-plot column cartridges. About 50 mg of the material were used in each test. The sample was supported on a plug of quartz wool, approximately 5 mm in height, which was placed on top of a distributor plate inside the quartz reactor. In a cyclic experiment, the material was exposed to the following atmospheres: (i) 5 min N₂ (100 mL min^{-1}), (ii) 30 min of reduction under a flow of 10 vol.% CH₄ and 10 vol.% CO₂ in N₂ (10 mL min^{-1}), (iii) 10 min N₂ (100 mL min^{-1}), (iv) 20 min oxidation with 6 vol.% steam in N₂, and (v) 10 min of oxidation in 5% O₂ in N₂ (100 mL min^{-1}). These redox steps were repeated over 10 cycles. The effluent gas leaving the reactor was passed first through a cold trap to condense out water and subsequently analyzed by the micro-GC. Inert N₂ was used as internal standard. Thus, the change in the N₂ concentration during the reaction allows us to estimate the volumetric total flow rate of the off-gas as following:

$$F_{\text{outlet}} = \frac{C_{\text{N}_2, \text{inlet}}}{C_{\text{N}_2, \text{outlet}}} \times F_{\text{inlet}}$$

Hence, the conversion of methane was calculated from the CH₄ concentration and the total flow rate in the off-gas:

$$X_{\text{CH}_4} = 1 - \frac{F_{\text{outlet}} \times C_{\text{CH}_4, \text{outlet}}}{F_{\text{inlet}} \times C_{\text{CH}_4, \text{inlet}}}$$

where, F , C , and X represent volumetric flow rate, concentration and

conversion, respectively.

2.4. Operando XRD - Fe XAS and in situ Pt XAS measurements

X-ray absorption spectroscopy (XAS) and X-ray powder diffraction (XRD) experiments were performed at the Swiss–Norwegian Beamlines (SNBL, BM31) at the European Synchrotron Radiation Facility (ESRF) in Grenoble, France. XAS spectra were collected at the Fe K-edge and Pt L_{III}-edge using a double-crystal Si (111) monochromator (continuous scanning in transmission mode). XRD data were collected with a 2D DEXELA [24] detector and a Si (111) channel-cut monochromator set at a wavelength of 0.5050 Å. XAS and XRD data were collected in the same capillary cell.

First a (*operando*) XRD experiment was carried out, then a new fresh sample was used to study the material by (*operando*) Fe K-edge XAS. In these experiments, the capillary cell was filled with ~ 5 mg of material and heated to 750 °C under He (25 mL/min). A mixture of CH₄/CO₂ (1:1, 10 vol.% in N₂, 10 mL/min) was used for DRM tests. The effluent gas leaving the capillary cell was passed first through a cold trap to condense out water and subsequently analyzed by micro-GC (Thermo Scientific C2V-200 micro-Gas Chromatograph, described in the previous section). A schematic of the setup is presented in Fig. S5.

Pt L_{III}-edge (*in situ*) XAS experiments were conducted on CeO₂-Pt. The following experiments were carried out: i) The sample was heated to 750 °C in He and subsequently exposed to DRM conditions. After 10 and 120 min of time on stream the material was cooled down to 150 °C and EXAFS data were collected (to reduce the effect of atomic thermal vibrations). After DRM, the material was exposed to air for 30 min and XAS data were collected after cooling down to 150 °C. ii) Additionally, to study the effect of DRM conditions on the structure of the Pt particles the following control experiment was performed: a fresh CeO₂-Pt sample was heated to 750 °C in He and subsequently exposed to a H₂ atmosphere (5 vol.% in He). After 120 min of time on stream the material was cooled down to 150 °C and EXAFS data were collected.

In the following, the term *operando* is used when the measurements were done under reaction working conditions (at 750 °C under a mixture of CH₄:CO₂ = 1:1) while simultaneously monitoring the reaction products by GC. The term *in situ* is used when the measurements were performed in the capillary reactor after cooling down to room temperature (to reduce thermal vibrations).

EXAFS (extended X-ray absorption fine structure) data processing and analysis were performed using the IFFEFIT package, included in the Athena software for spectral normalization, background subtraction, *k*-weighting, Fourier Transformation and linear combination analysis. [25] The Artemis software was used to fit the EXAFS data. The structural parameters, *i.e.* the inter-atomic distances, coordination numbers and the Debye–Waller factors were obtained by nonlinear least-squares fitting of the *k*²-weighted EXAFS functions in the *k*-range of 3–10 Å^{−1}. Single scattering paths were calculated using the FEFF6 code integrated in the Artemis software. [25,26] The continuous Cauchy Wavelet Transform (WT) of the EXAFS data was performed using a Matlab script released by Muñoz et al. [27].

3. Result and discussion

3.1. Thermodynamic assessment

DRM is an endothermic reaction (CH₄ + CO₂ ↔ 2CO + 2H₂, ΔH_{298K} = +247 kJ mol^{−1}), which requires high temperatures to attain high equilibrium conversions of CH₄ and CO₂ to a synthesis gas. The synthesis gas produced is expected to reduce Fe₂O₃ to metallic Fe. Depending on the operating temperature and partial pressure of the reactants, side reactions may occur. The thermodynamic equilibrium data (Fig. 2a) of the DRM reaction was derived by minimizing the Gibbs free energy of a system containing the species CH₄, CO, CO₂, H₂ and H₂O (with CH₄ and CO₂ being the only educts according to the DRM

reaction). The Fe–O phase diagram as a function of temperature and partial pressure of oxygen, *p*_{O₂}, at 1 atm is shown in Fig. 2b to illustrate the thermodynamically stable oxidation states of iron for the respective gas environments. From Fig. 2b, a conversion of CH₄ > 40% is required to generate a gas mixture with a *p*_{O₂} sufficiently low to reduce Fe₂O₃ to metallic Fe. At 750 °C, the conversion of CH₄ is predicted to be ~ 95%, allowing for a complete reduction of Fe₂O₃ to metallic Fe (Fig. 2b). However, in the absence of a catalyst, the conversion of CH₄ and CO₂ to synthesis gas is much lower (usually < 5%). [23] The resulting gas mixture, consisting mainly of unconverted CH₄ and CO₂, would prevent a reduction of the iron oxide beyond the Fe₃O₄ oxidation state.

3.2. Materials characterization

The SEM images of the different synthesis steps of the core shell Fe₂O₃@CeO₂ material, starting with Fe₃O₄ microspheres (as described in the experimental section), are shown in Fig. S2. The CeO₂ loading in Fe₂O₃@CeO₂ was determined as 35 wt.% by inductively coupled plasma optical emission spectroscopy (ICP-OES). In good agreement with these results, the Rietveld refinement of the XRD data of Fe₂O₃@CeO₂ yielded a phase composition of 64 wt.% α-Fe₂O₃ and 36 wt.% CeO₂ (Fig. S1a and Table S1). The Pt content in the Fe₂O₃@CeO₂-Pt material was determined as 1 wt.% by ICP-OES. A scanning electron micrograph (SEM) of Fe₂O₃@CeO₂-Pt is presented in Fig. 3a, showing regular sub-micrometer particles (~400 nm) of spherical shape. The HAADF-STEM and the corresponding EDS maps show the elemental distribution and structure of the bifunctional material (Fig. 3b and c), revealing the core-shell structure, with a core of iron oxide and a shell formed by CeO₂ particles. In the high resolution HAADF-STEM image (Fig. 3d), a Pt nanoparticle on the CeO₂ shell can be visualized, while the average Pt particle size was determined as ~1 nm, Fig. S12.

Additionally, the SEM of the reference sample prepared by co-precipitation, named as Fe₂O₃-CeO₂-Pt shows a different morphology from the core-shell material. Fe₂O₃-CeO₂-Pt was composed of Fe₂O₃ and CeO₂ polyhedron-shaped particles (diameter: 50–100 nm) as shown in Fig. S3a. HAADF-STEM and the corresponding EDS mapping (Fig. S3b) revealed that the Pt NPs were deposited on both CeO₂ and Fe₂O₃ surfaces unlike in Fe₂O₃@CeO₂-Pt, in which Pt NPs were found on CeO₂ only.

3.3. DRM-CLH experiments

The concentration of the off-gas from the packed bed measured during the first redox cycle using Fe₂O₃@CeO₂-Pt is plotted in Fig. 4a. In the initial stage of the DRM step (when the Fe₂O₃ particles were reduced), an increase in the concentration of CO₂ was observed due to the reduction of Fe₂O₃ by CO, as revealed by *operando* XRD (Section 3.4). At the end of the DRM step (after 30 min), the conversion of CH₄ was determined as ~ 85%. In the CLH step, H₂ was produced close to the theoretically expected value (considering the reduction of Fe₂O₃ to Fe) of 10.8 mmol/g catalyst-oxygen carrier, while no CO₂ or CO were detected, resulting in pure H₂ on a N₂- and steam-free basis. The detection limit of the overall CO contamination in our micro-GC was of the order of 2 ppm.

The redox performance of the co-precipitated reference material Fe₂O₃-CeO₂-Pt is presented in Fig. 4b. For this material, Fe₂O₃ was not reduced fully under DRM conditions and indeed no H₂ was produced in the subsequent steam oxidation step (Fig. 4b). The conversion of CH₄ for Fe₂O₃-CeO₂-Pt (~ 10%) was considerably lower than that of Fe₂O₃@CeO₂-Pt (~ 85%), resulting in a reduction of Fe₂O₃ to Fe₃O₄ only (according to XRD shown in Fig. S4a). This result is in line with our thermodynamic calculations (Fig. 2). For a low DRM activity (CH₄ conversion < ~ 40%) Fe₃O₄ is predicted to be the stable oxide. The poor DRM performance of Fe₂O₃-CeO₂-Pt can be related to the lower DRM activity of Pt nanoparticles supported on Fe₂O₃, possibly due to the

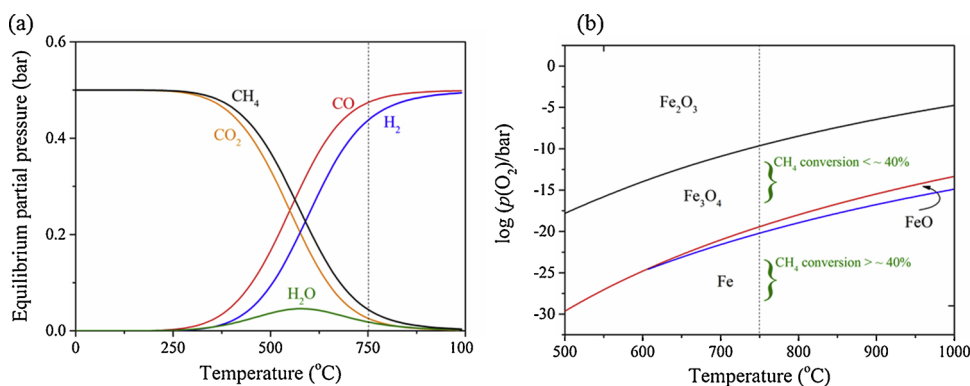


Fig. 2. (a) Thermodynamic equilibrium plots of the DRM at 1 atm, for the temperature range 0–1000 °C using an inlet feed ratio of $\text{CO}_2/\text{CH}_4 = 1$ (carbon formation is neglected). (b) Equilibrium phase diagram for the oxides of iron. The data plotted was computed by minimizing the total Gibbs free energy of the respective system using standard thermodynamic tables. [28] The dashed line represents a temperature of 750 °C, i.e. the testing temperature of the material.

formation of an iron oxide film on top of Pt as reported previously. [29] Overall, the material $\text{Fe}_2\text{O}_3@\text{CeO}_2\text{-Pt}$ had a much better performance for DRM-CLH than the material prepared by co-precipitation, i.e. $\text{Fe}_2\text{O}_3\text{-CeO}_2\text{-Pt}$. Hence, our further characterizations focused on the core-shell material $\text{Fe}_2\text{O}_3@\text{CeO}_2\text{-Pt}$. It is noted that the control experiment using the sample without Pt, viz. $\text{Fe}_2\text{O}_3@\text{CeO}_2$, showed no DRM reactivity (Fig. 4c), which demonstrates that the DRM reaction in the experiment using $\text{Fe}_2\text{O}_3@\text{CeO}_2\text{-Pt}$ has effectively allowed the reduction of Fe_2O_3 using CH_4 and CO_2 . The cyclic stability and redox performance of the catalyst-oxygen carrier were assessed further in a fixed-bed reactor at 750 °C. The composition of the off-gas recorded over multiple redox cycles is plotted in Fig. S4b. The conversion of CH_4 and CO_2 during the DRM step and the yield of H_2 are plotted as a function of cycle number in Fig. 4d. The bifunctional material $\text{Fe}_2\text{O}_3@\text{CeO}_2\text{-Pt}$ has a high catalytic activity for DRM and also a high H_2 yield (~ 10.8 mmol/g oxygen carrier) over 10 redox cycles.

3.4. Structural changes during DRM-CLH

Operando synchrotron XRD and Fe K-edge XAS were conducted to determine the structural changes of $\text{Fe}_2\text{O}_3@\text{CeO}_2\text{-Pt}$ during multiple DRM-CLH cycles. In these experiments, a quartz capillary served as the reactor (using CH_4/CO_2 (1:1), 10 vol.% in N_2 for DRM, and CO_2 and air for oxidation at 750 °C). The composition of the gas at the outlet of the reactor cell was analyzed by a micro-GC (Fig. S5). Due to the experimental limitations of the setup, CO_2 was used as oxidant in the CLH step, since it has a similar oxidation potential as steam at 750 °C. The XRD patterns collected during the DRM step (Figs. 5a and S6a) show the formation of metallic Fe through Fe_3O_4 and FeO intermediates, while the off-gas analysis (Fig. 5b) shows a high DRM activity and an increase in the CO_2 concentration during the reduction of Fe_2O_3 , according to $3\text{Fe}_2\text{O}_3 + \text{CO} \rightarrow 2\text{Fe}_3\text{O}_4 + \text{CO}_2$. It was not possible to record the evolution of H_2O during the measurement, but it is expected that H_2O was produced during reduction, according to $3\text{Fe}_2\text{O}_3 + \text{H}_2 \rightarrow 2\text{Fe}_3\text{O}_4 + \text{H}_2\text{O}$. The combined XRD and off-gas profile analysis identified three distinct reaction stages: (i) sequential reduction of $\text{Fe}_2\text{O}_3 \rightarrow \text{Fe}_3\text{O}_4 \rightarrow \text{FeO}$ leading to an initial increase in the concentration of CO_2 (maximum of 7 vol.%

after 8 min of time on stream); (ii) reduction $\text{FeO} \rightarrow \text{Fe}$ leading to a comparatively stable concentration of CO_2 of approximately 4 vol.% (lasting for ~ 5 min). The reduction of $\text{FeO} \rightarrow \text{Fe}$ was found to be the slowest reduction step, which is in agreement with previous studies; [30] (iii) When all of the FeO was reduced to Fe, the CO_2 concentration decreased to 1 vol.%, with a simultaneous stabilization of the concentrations of H_2 and CO at 11.5 and 12 vol.%, respectively. Once the reduction of the bi-functional material was complete, the conversion of CH_4 was determined as 90%.

Operando XANES data (Fig. S6b) and the corresponding linear combination fitting (LCF) analysis (Fig. 5c) confirm that the reduction of Fe_2O_3 to Fe proceeded through Fe_3O_4 and FeO intermediates. A comparison of the XANES spectra collected after 30 min of the DRM reaction with the Fe foil reference spectrum demonstrates that Fe_2O_3 was reduced completely to metallic Fe. Note that the full reduction of Fe_2O_3 to Fe is key to achieve the maximal yield of H_2 per unit mass of oxygen carrier. Moreover, in this experiment, the formation of a CeFeO_3 perovskite phase was not observed by XRD, and the XANES data was fitted successfully with the Fe_2O_3 , Fe_3O_4 and FeO references. This observation is important because the formation of CeFeO_3 has been reported previously as a possible deactivation mechanism for Fe-Ce-based oxygen carriers, since CeFeO_3 is non-reducible (to Fe) at temperatures below 750 °C. [31,32]

Rietveld analysis was conducted to gain more information on the structure of the CeO_2 shell and its chemical stability under DRM conditions. Analysis of the CeO_2 lattice parameters during DRM (Fig. 5d) shows an increase during the first stage of the DRM step, subsequently, the lattice parameters remained stable over time. This increase in the cell parameter of CeO_2 can be related to a partial reduction of CeO_2 (CeO_{2-x}) since Ce^{3+} has a larger ionic radius than Ce^{4+} [33].

In a control experiment, $\text{Fe}_2\text{O}_3@\text{CeO}_2\text{-Pt}$ was reduced in 10 vol.% H_2 in N_2 to investigate the rate of CeO_2 reduction in an atmosphere with a higher reduction potential than a DRM mixture. From Fig. 5d, it can be seen that in a H_2 atmosphere the lattice parameters of CeO_{2-x} increased more than under DRM conditions, indicative of a slower reduction of Ce^{4+} under DRM conditions than under H_2 . Ce K-edge XAS data (Fig. S6d) also showed a shift in the edge position from 40,471 eV

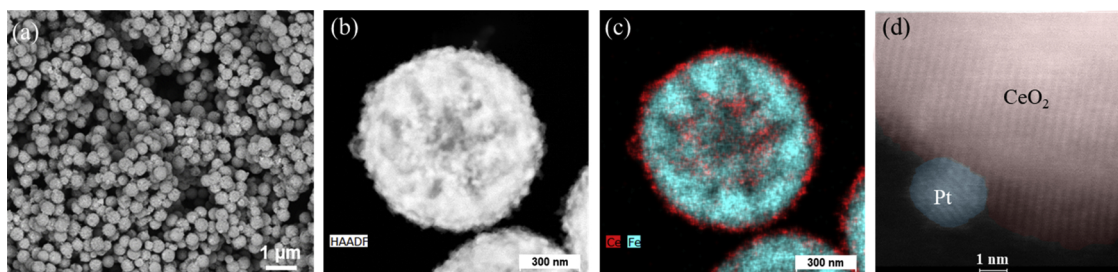


Fig. 3. (a) SEM image of the as-synthesized $\text{Fe}_2\text{O}_3@\text{CeO}_2\text{-Pt}$, (b) HAADF-STEM image of $\text{Fe}_2\text{O}_3@\text{CeO}_2\text{-Pt}$ (c) Elemental mapping of $\text{Fe}_2\text{O}_3@\text{CeO}_2\text{-Pt}$ with EDS, (d) High resolution HAADF-STEM image of a Pt nanoparticle on the CeO_2 shell.

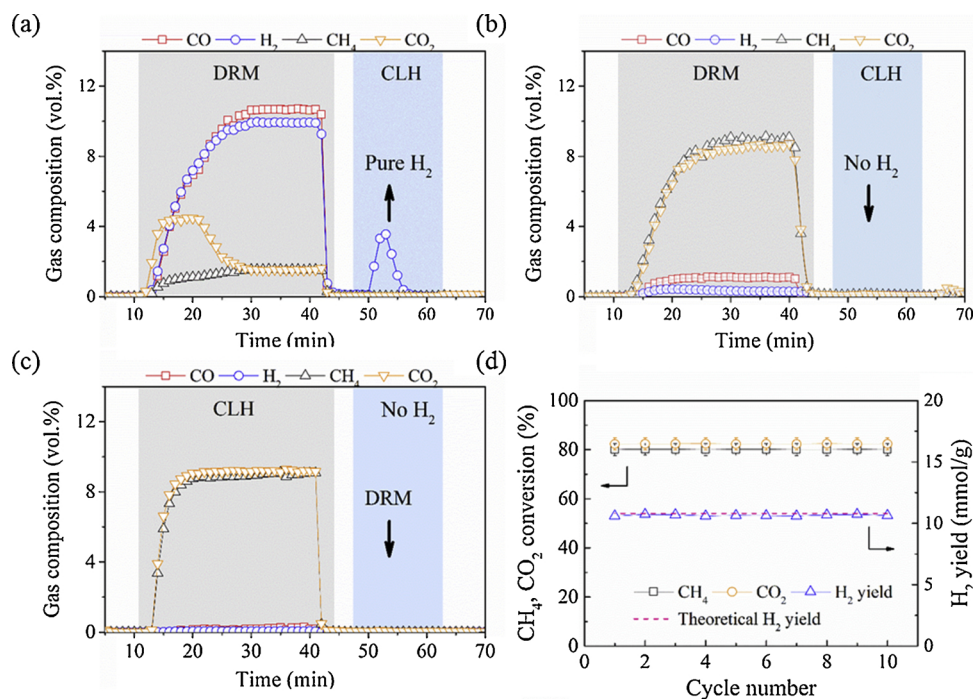


Fig. 4. Integrated DRM-CLH process using $\text{Fe}_2\text{O}_3@ \text{CeO}_2\text{-Pt}$ in a fixed-bed reactor at 750°C . In the reduction step (of the oxygen carrier) a mixture of CH_4/CO_2 (1:1) was used and the materials were oxidized first with 6 vol.% steam in N_2 , followed by air. (a) $\text{Fe}_2\text{O}_3@ \text{CeO}_2\text{-Pt}$ core-shell structure, (b) $\text{Fe}_2\text{O}_3\text{-CeO}_2\text{-Pt}$ synthesized by co-precipitation. (c) $\text{Fe}_2\text{O}_3@ \text{CeO}_2$ core-shell structure (d) The yield of H_2 and the conversion of CO_2 and CH_4 are plotted as a function of cycle number for the sample $\text{Fe}_2\text{O}_3@ \text{CeO}_2\text{-Pt}$. The redox experiments were performed using the same conditions as in (a). The error bars represent two standard deviations based on measurements obtained during the last five minutes of the DRM reaction.

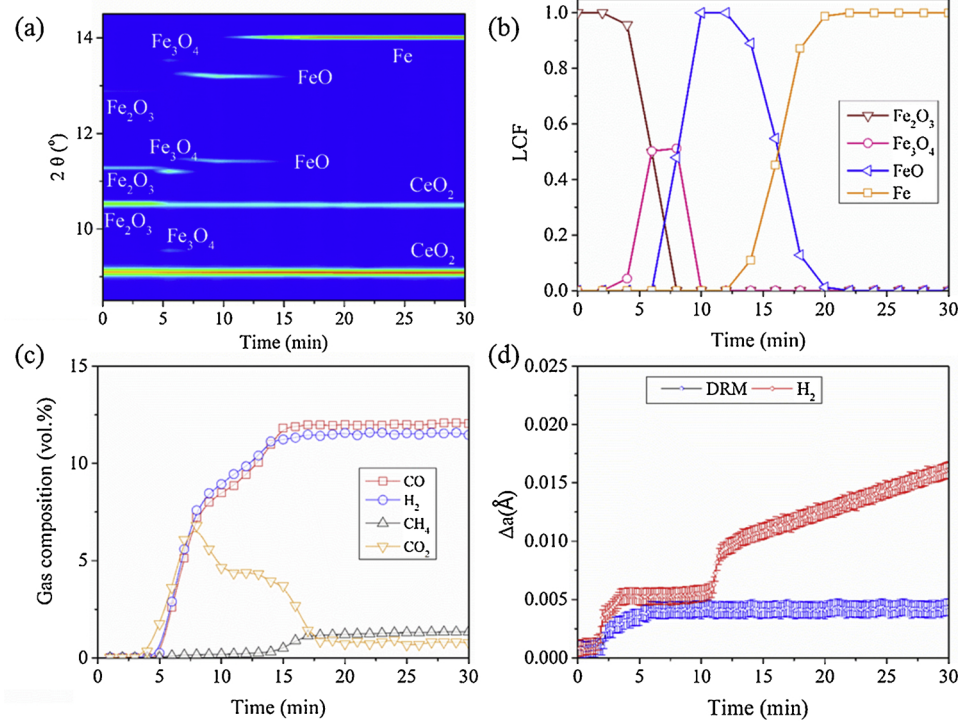
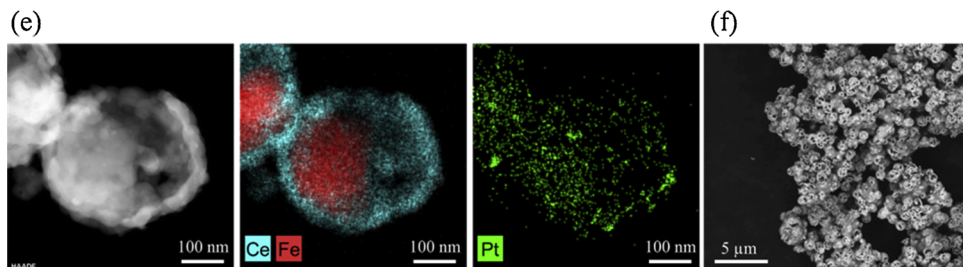


Fig. 5. Operando experiments: time resolved XRD (a) and micro-GC data (b) for $\text{Fe}_2\text{O}_3@ \text{CeO}_2\text{-Pt}$ using a mixture of CH_4/CO_2 (1:1, 10 vol.% in N_2 at 750°C) in a quartz capillary reactor. (c) LCF analysis calculated from operando XANES data giving the fraction of iron in Fe_2O_3 , Fe_3O_4 , FeO and Fe as a function of time on stream. (d) Changes of the CeO_2 lattice parameter calculated from the diffraction patterns in (a); $\Delta a = a_t - a_0$, where a_0 and a_t are the CeO_2 lattice parameter at the beginning of the experiment (under air) and at time 't' on stream, respectively. To compare the rate of reduction of CeO_2 in an atmosphere with a higher reduction potential than a DRM mixture, a similar experiment was performed using H_2 for reduction instead of a mixture of CH_4/CO_2 . The error bars represent standard deviations based on measurements obtained by Rietveld refinement. (e) Imaging of the reduced (reduced) $\text{Fe}_2\text{O}_3@ \text{CeO}_2\text{-Pt}$ by HAADF-STEM and the corresponding elemental maps. (f) SEM image of the cycled (oxidized) $\text{Fe}_2\text{O}_3@ \text{CeO}_2\text{-Pt}$.



towards lower energies after H_2 treatment. Such a shift is indicative of the partial reduction of CeO_2 . As the core-hole lifetime broadening effect becomes appreciable for heavy atoms at the K-edge, we were not able to provide any quantitative information on the ratio Ce^{3+}/Ce^{4+} [34]. Nonetheless, it can be observed that the shift in the edge position under DRM conditions was appreciably smaller when compared to a H_2 atmosphere, in agreement with XRD analysis. Moreover, it is noted that under the conditions applied in this experiment, the perovskite-type $CeFeO_3$ phase was not formed, probably due to kinetic limitations and the limited degree of reduction of Ce^{4+} to Ce^{3+} , since $CeFeO_3$ formation requires a high concentration of Ce^{3+} [35–37].

Turning to the oxidation step, from the XRD patterns collected during CO_2 and air oxidation (Figure S7), it was found that in a CO_2 atmosphere the material was oxidized to Fe_3O_4 (as expected from thermodynamics) and to Fe_2O_3 in the subsequent air oxidation step. Therefore, an air oxidation step is required to regenerate fully the reduced materials.

The reference sample, $Fe_2O_3@CeO_2$ (i.e. without Pt NPs), was examined under similar reaction conditions (CH_4/CO_2 (1:1)). As shown in Fig. S8, Fe_2O_3 in this material was not reduced beyond Fe_3O_4 in a mixture of CO_2 and CH_4 . This observation demonstrates that the presence of DRM-active Pt nanoparticles is critical to yield a synthesis gas that has a sufficiently high reduction potential to reduce Fe_2O_3 to metallic Fe at a fast rate.

To probe the morphological changes over repeated redox cycles, HAADF-STEM and SEM images (Fig. 5e and f, respectively) of the cycled (reduced) materials were acquired. It was found that the spherical structure of the encapsulated oxygen carrier was preserved and Pt nanoparticles (~2 nm) were homogeneously distributed on CeO_2 (Fig. S9).

3.5. DRM on CeO_2 -supported Pt nanoparticles

In the bifunctional material, the Pt NPs supported on CeO_2 acted as the DRM catalyst, converting CH_4 and CO_2 to H_2 and CO. Hence, characterizing the catalytic activity and the structure of the Pt NPs under DRM conditions is important to improve the material's performance. In a coupled DRM-CLH experiment the simultaneous occurrence of the reduction of iron oxide ($3Fe_2O_3 + CO \rightarrow 2Fe_3O_4 + CO_2$, $3Fe_2O_3 + H_2 \rightarrow 2Fe_3O_4 + H_2O$) and the DRM reaction makes a detailed characterization of the material's activity for DRM very complex. Hence, in the following the DRM activity is studied using iron-free samples, i.e. Pt supported on CeO_2 .

DRM-oxidation cycles were performed in a fixed-bed reactor at 750 °C with the results shown in Fig. S10. In each cycle, the material was exposed first to a mixture of CH_4/CO_2 (1:1), followed by steam and air oxidation. In the first cycle, after 60 min, the material possessed a high DRM activity producing a synthesis gas with a $H_2:CO$ molar ratio of 0.9. The measured $H_2:CO$ ratio was less than unity due to the simultaneous occurrence of the reverse water gas shift (RWGS) reaction. It was found that the catalyst activity decayed progressively with time (Fig. S10). This decay could have been due to either the sintering of Pt nanoparticles and/or coke deposition. Based on a reference experiment in a TGA (Fig. S11), we could rule out carbon deposition as a deactivation mechanism, since the sample weight did not increase under DRM conditions for 60 min. After the oxidation step, the Pt catalyst recovered its initial activity in the second and third cycles, with a similar trend of a decaying activity in each cycle. Therefore, the DRM activity of Pt was retained over multiple redox cycles. A possible explanation for the regeneration of the catalytic activity of the material is the re-dispersion of Pt nanoparticles on the CeO_2 support during re-oxidation. [38]

To shed light on the cause of deactivation and regeneration, HAADF-STEM images (Fig. 6) of the as-synthesized and spent CeO_2 -Pt catalyst (after DRM and regeneration) were acquired. The STEM image of the as-synthesized catalyst (Fig. 6a) shows highly dispersed Pt nanoparticles on CeO_2 , with an average particle size of ~1 nm (Fig. S12). Fig. S12 shows HAADF-STEM images of the CeO_2 -Pt materials with the

corresponding histograms of Pt particle size distribution (see also chemisorption results presented in Table S2).

Exposing the material to DRM conditions for 10 min and 60 min, larger Pt NPs (~2 nm and ~4 nm, respectively) were formed (Figs. 6b and c and S12), revealing that Pt NPs sintered and probably caused the observed catalytic deactivation during one DRM cycle. After oxidative treatment with steam followed by air, we could not detect any Pt NPs on the surface of the catalyst (Fig. 6d). This is related to the oxidation of Pt and the high mobility of platinum oxide species on the surfaces of CeO_2 . The oxidation of Pt NPs was confirmed by XAS analysis (see below in Fig. 7). Contrasted features marked by circles in Fig. 6e were probably oxidic platinum species dispersed on the CeO_2 surface. It should be noted that in a HAADF-STEM image the contrast is related to the elemental composition, with the intensity being proportional to the atomic number. [39,40] EDS analysis of the CeO_2 -Pt catalyst showed a highly homogeneous distribution of Pt on the CeO_2 surface after air oxidation (Fig. 6f). After the second DRM cycle (10 min and 60 min of time on stream), the Pt NPs became visible again (Fig. 6g and h). They had a similar average size as the Pt NPs observed after the first cycle (Fig. 6b and c), with the growth of the size of the Pt particles being again the cause for catalyst deactivation with TOS. The re-dispersion of Pt during oxidation in air (through platinum oxide species) was demonstrated indirectly by the catalytic activity of the material, as the initial CH_4 conversion in the first reduction step was restored in the second reduction step. The average Pt particle size as a function of time on stream is plotted for the first and second DRM cycle in Fig. 6i. These measurements confirmed that oxidation in air resulted in smaller Pt particles counteracting sintering. H_2 chemisorption was used to determine the dispersion of the Pt NPs (Table S2). It was found that after reduction in H_2 at 750 °C the dispersion of Pt NPs was small due to sintering. After oxidation in air a high dispersion was restored, in agreement with the electron microscopy observations in Fig. 6.

Aiming at understanding better the local structure of Pt under DRM and oxidative conditions and to elucidate possible metal support interactions, *in situ* Pt L_{III}-edge XAS experiments were conducted on CeO_2 -Pt. The X-ray absorption near-edge structure (XANES) region of the spectra of CeO_2 -Pt and the references (Pt foil and α -PtO₂) are shown in Fig. 7a. As reported previously, the intensity of the XANES white line is proportional to the oxidation state of Pt. [41] The oxidation state of the as-synthesized Pt was close to metallic Pt⁰ and this state did not change during DRM. After oxidation in air, the intensity of the white line increased, indicating that Pt was partially oxidized. These observations were confirmed by EXAFS analysis. Fig. 7b shows Fourier-transformed EXAFS functions of the as-synthesized and reacted catalysts. Fourier-transformed EXAFS functions of the references (Pt foil and α -PtO₂) and the catalyst (acquired *in situ* after H_2 treatment for 120 min) are also shown in Figs. 7d and S13, respectively. After air oxidation, the Pt-O interaction at ~1.5 Å in the FT appeared, indicating that the Pt nanoparticles were partially oxidized, in agreement with the XANES data. Additional structural information was obtained by EXAFS fitting and Wavelet transform (WT) analysis. [27] WT analysis provides a correlation between real, R-space (where R is the distance from the absorber atom), and, k-space (where k is the photoelectron wave-number). Since the contributions of scattering neighbors with different atomic numbers to the EXAFS signal are localized differently in k-space, WT analysis allows to distinguish between two different atoms positioned at similar distances from Pt. Therefore, this analysis is particularly useful to investigate Pt-support interactions. As can be observed in Fig. 7d and a feature centered at ~2.7 Å in the WT plots and in the k range of 8–9 Å⁻¹, corresponding to Pt-Pt scattering, appeared in all of the materials exposed to H_2 , air and DRM (after 10 min or 120 min). Additionally, a feature at lower k-values (6–7 Å⁻¹, partly overlapping with the Pt-Pt feature marked by dotted circles) was observed under air and DRM conditions (Fig. 7d). Atoms with lower atomic numbers are more efficient backscatterers at low k-values compared to higher atomic numbers atoms. [27] Therefore, the 'lower k' feature can be

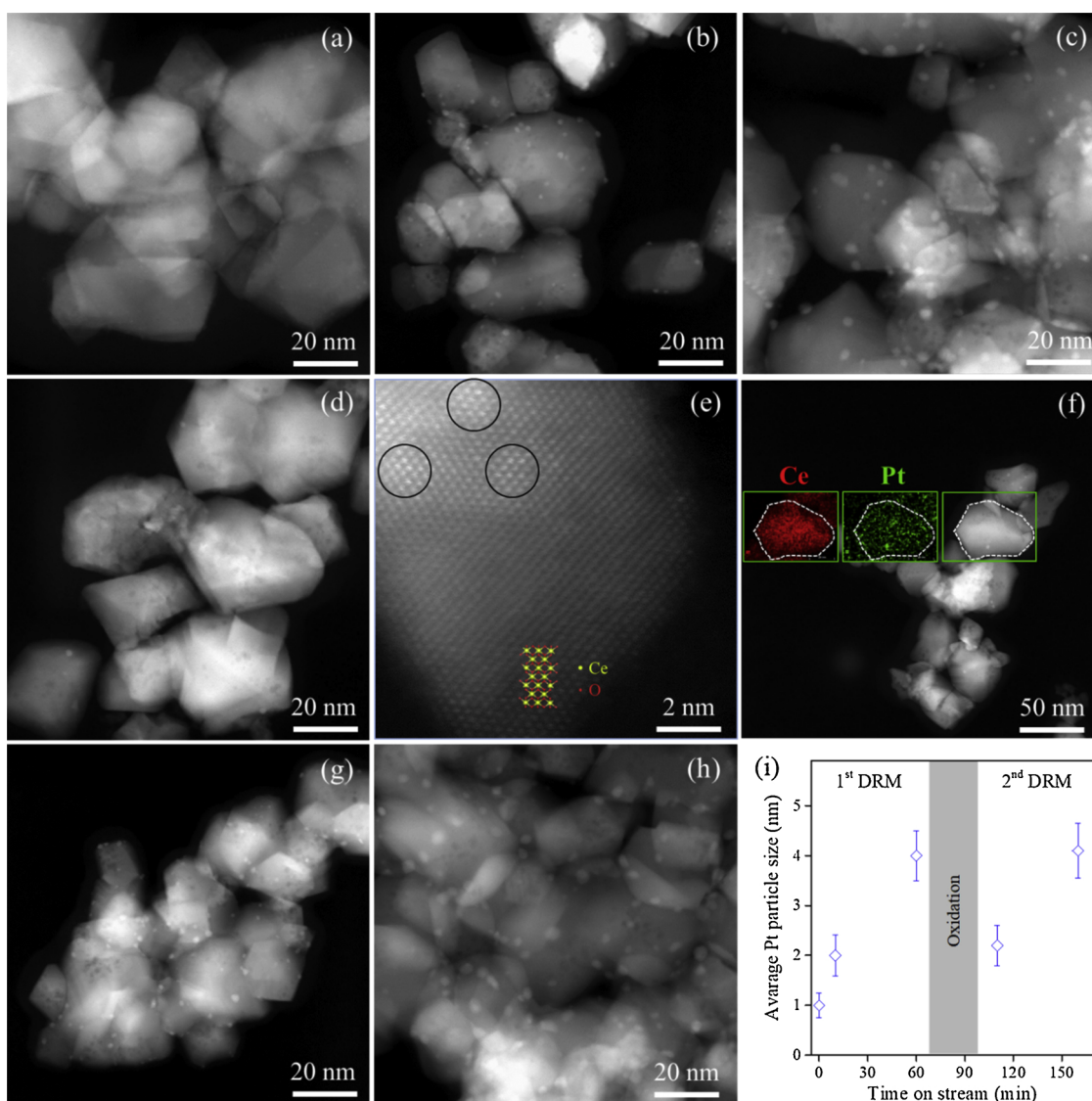


Fig. 6. CeO₂-Pt catalyst: HAADF-STEM images of (a) as-synthesized, (b) after first DRM cycle (10 min), (c) after first DRM cycle (60 min), (d) after re-oxidation; (e) high resolution HAADF-STEM image and (f) elemental mapping using EDS after re-oxidation; HAADF-STEM images of (g) after second DRM cycle (10 min), (h) after second DRM cycle (60 min). (i) Average Pt particle size as a function of time on stream for the first and second cycles. The particle size distribution obtained using 160 particles is shown in Figure S12. The materials were exposed to the following DRM conditions: CH₄/CO₂ = 1:1 (10 vol.% in N₂) for 60 min and re-oxidized with steam and air at 750 °C.

related to the interaction of the Pt NPs with the CeO₂ support. After 60 min of DRM, this feature became less intense with time, indicating that there was a decrease of the Pt-CeO₂ interaction with time on stream. Moreover, this feature was very weak for the sample collected under H₂ treatment.

These observations are confirmed and rationalized by EXAFS fittings (Fig. S14 and Table S3). In these fittings, one Pt-Pt scattering path was used to model the first shell around Pt and an additional scattering path for Pt-Ce was added to obtain a good fit for the sample exposed to DRM conditions. The main observations of the EXAFS fitting were: (i) A linkage between Pt and Ce (at 3.2 Å) must be considered to fit well the EXAFS data of a material that has been exposed to DRM conditions; (ii) After H₂ treatment, this linkage was less evident and the EXAFS data could be fitted without considering a Pt-Ce path. As shown by XRD analysis (Section 3.4), a higher degree of CeO₂ reduction was observed during H₂ treatment. Thus, the decrease in the Pt-Ce interaction under H₂ compared to DRM is linked to the higher degree of the (partial) reduction of Ce⁴⁺ to Ce³⁺, which resulted in the breaking of the Pt-support interaction; (iii) The interaction Pt-Ce weakened with time

on stream during DRM, as evidenced by a decrease in the coordination number of Pt-Ce (from 1.1 after 10 min to 0.2 after 120 min), and is also supported by EXAFS WT analysis (Fig. 7d). A weakening of the Pt-Ce interaction lead to the sintering of Pt nanoparticles, as supported by an increase of the coordination number of Pt-Pt from 6.7 to 7.4 and HAADF-STEM imaging (Fig. 6); (iv) After oxidation in air, a Pt-O interaction was observed (at 1.9 Å) and the Pt-Ce interaction became stronger as evidenced by an increase in the coordination number for Pt-Ce (from 0.2 to 0.9), while the Pt-Pt coordination number decreased from 7.4 to 6.5. In line with TEM measurements, this observation suggests a re-dispersion of Pt NPs during oxidation in air. A longer exposure time to air is expected to lead to a higher degree of oxidation of platinum and hence better re-dispersion.

4. Conclusions

In conclusion, we have developed a bifunctional material Fe₂O₃@CeO₂-Pt for the production of pure H₂ on a N₂- and steam-free basis, utilizing a mixture of CO₂/CH₄ by integrating the DRM into a

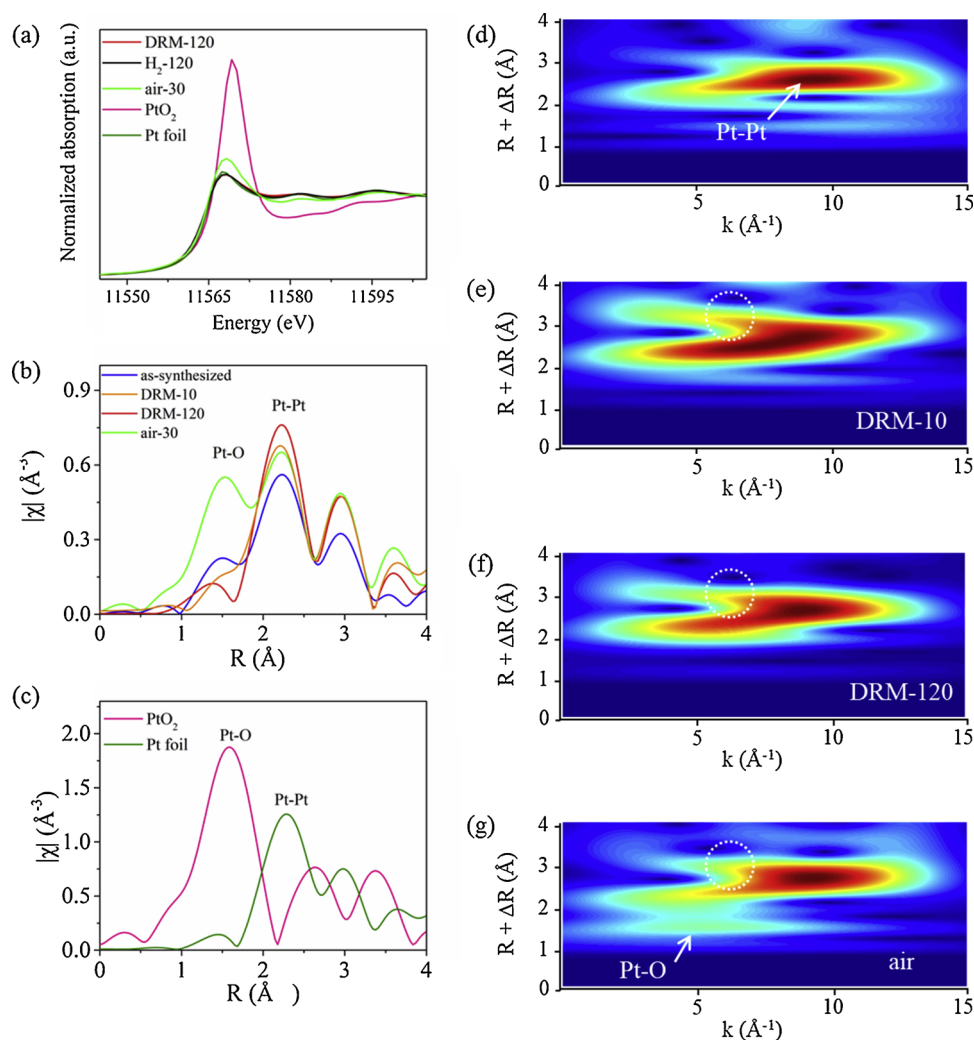


Fig. 7. Pt L_{III} -edge XANES spectra (a) and Fourier transformed EXAFS functions (not corrected for phase shift) of (b) CeO_2 -Pt under DRM (after 10 min or 120 min), air (30 min) or H_2 (120 min) conditions. Fourier transformed EXAFS data for H_2 treatment (120 min) is given in Fig. S13. (c) Fourier transformed EXAFS of the references (Pt foil and α - PtO_2), Wavelet transform (WT) analysis of the EXAFS data: Pt Foil, (d) DRM after 10 (e) 120 min (f), and after air (30 min) (g).

chemical looping-based H_2 production scheme. While other research has previously demonstrated the feasibility of the coupling of the two processes (DRM and CLH) with spatially separated particle systems, we show that the coupling can be realized on a particle scale, provided the catalyst-oxygen carrier material is designed carefully. The addition of 1 wt.% Pt yielded a material with a high DRM activity and coke resistance. This provided a stream of synthesis gas that reduced simultaneously iron oxide to metallic Fe. In the subsequent steam oxidation cycle, the bifunctional material achieved very high H_2 yields (close to theoretical expected value of 10.8 mmol/g catalyst-oxygen carrier). The cyclic stability was very high over the 10 redox cycles tested. *Operando* XRD and XANES measurements using $Fe_2O_3@CeO_2$ -Pt demonstrated that under DRM conditions Fe_2O_3 was reduced fully to Fe through the Fe_3O_4 and FeO intermediates.

Although we observed, in a second set of experiments, that the activity of CeO_2 supported Pt catalysts decayed with time on stream under DRM conditions due to sintering of Pt nanoparticles, the activity was restored after the oxidation step, thus ensuring a high cyclic stability. Re-dispersion of Pt nanoparticles via mobile platinum oxide species that formed during air oxidation allowed for the regeneration of the catalytic activity within a redox cycle. HAADF-STEM, XANES and EXAFS analysis of the materials, complemented by a wavelet transform analysis of the EXAFS data (L_{III} -edge), elucidated the interaction of Pt with CeO_2 under a redox environment. The observed oxidation-metal-

support interaction/re-dispersion mechanism provides an efficient means of counteracting particle sintering, yielding a cyclically highly active material. Therefore, the air oxidation step is not only necessary to restore the Fe_2O_3 core, but it is key to maintain a stable catalytic performance and, consequently, cyclic operation.

Declaration of Competing Interest

The authors declare that they have no known competing financial interests or personal relationships that could have appeared to influence the work reported in this paper.

Acknowledgement

We would like to acknowledge support from the Swiss National Science Foundation (Project IZERZO_141976). Dr. P.M. Abdala would like to acknowledge ETH SEED grant (SEED-02 17-2). We also thank the Scientific Centre for Optical and Electron Microscopy (ScopeM) for providing training on and access to electron microscopes. ESRF and the Swiss Norwegian Beamlines (SNBL at ESRF) are acknowledged gratefully for providing access to the synchrotron facility. Dr. Michela Brunelli is acknowledged for her support and valuable discussions during XRD and XAS measurements at MB31 beamline (ESRF). We thank Dr. Agnieszka Kierzkowska for ICP-OES measurements and Dr.

Andac Armutlulu for SEM analysis.

Appendix A. Supplementary data

Supplementary material related to this article can be found, in the online version, at doi:<https://doi.org/10.1016/j.apcatb.2019.117946>.

References

- [1] A. Thursfield, A. Murugan, R. Franca, I.S. Metcalfe, Chemical looping and oxygen permeable ceramic membranes for hydrogen production-a review, *Synth. Lect. Energy Environ. Technol. Sci. Soc.* 5 (2012) 7421–7459.
- [2] C.S. Song, Fuel processing for low-temperature and high-temperature fuel cells - challenges, and opportunities for sustainable development in the 21st century, *Catal. Today* 77 (2002) 17–49.
- [3] L.-S. Fan, L. Zeng, W. Wang, S. Luo, Chemical looping processes for CO₂ capture and carbonaceous fuel conversion – prospect and opportunity, *Energy Environ. Sci.* 5 (2012) 7254.
- [4] J.P.E. Cleeton, C.D. Bohn, C.R. Muller, J.S. Dennis, S.A. Scott, Clean hydrogen production and electricity from coal via chemical looping: identifying a suitable operating regime, *Ind. Eng. Chem. Res.* 34 (2009) 1–12.
- [5] F. Garcia-Labiano, L.F. de Diego, P. Gayan, J. Adanez, A. Abad, C. Dueso, Effect of fuel gas composition in Chemical-Looping combustion with Ni-Based oxygen carriers. 1. Fate of sulfur, *Ind. Eng. Chem. Res.* 48 (2009) 2499–2508.
- [6] Z. Hausfather, Bounding the climate viability of natural gas as a bridge fuel to displace coal, *Energy Policy* 86 (2015) 286–294.
- [7] J.W. Hu, V.V. Galvita, H. Poelman, G.B. Marin, Advanced Chemical Looping Materials for CO₂ Utilization: A Review, *Materials* 11 (2018) 1187.
- [8] V.V. Galvita, H. Poelman, G.B. Marin, Hydrogen production from methane and carbon dioxide by catalyst-assisted chemical looping, *Top. Catal.* 54 (2011) 907–913.
- [9] V.V. Galvita, H. Poelman, C. Detavernier, G.B. Marin, Catalyst-assisted chemical looping for CO₂ conversion to CO, *Appl. Catal. B* 164 (2015) 184–191.
- [10] D. Pakhare, J. Spivey, A review of dry (CO₂) reforming of methane over noble metal catalysts, *Chem. Soc. Rev.* 43 (2014) 7813–7837.
- [11] F. Polo-Garzon, D. Pakhare, J.J. Spivey, D.A. Bruce, Dry reforming of methane on Rh-Doped pyrochlore catalysts: a steady-state isotopic transient kinetic study, *ACS Catal.* 6 (2016) 3826–3833.
- [12] Z. Xie, B. Yan, S. Kattel, J.H. Lee, S. Yao, Q. Wu, N. Rui, E. Gomez, Z. Liu, W. Xu, L. Zhang, J.G. Chen, Dry reforming of methane over CeO₂-supported Pt-Co catalysts with enhanced activity, *Appl. Catal. B* 236 (2018) 280–293.
- [13] Y. Nagai, K. Dohmae, Y. Ikeda, N. Takagi, T. Tanabe, N. Hara, G. Guilera, S. Pascarelli, M.A. Newton, O. Kuno, H. Jiang, H. Shinjoh, S. Matsumoto, In situ redispersion of platinum autoexhaust catalysts: an on-line approach to increasing catalyst lifetimes? *Angew. Chem. Int. Ed. Engl.* 47 (2008) 9303–9306.
- [14] J. Jones, H. Xiong, A.T. DeLaRiva, E.J. Peterson, H. Pham, S.R. Challa, G. Qi, S. Oh, M.H. Wiebenga, X.I. Pereira Hernandez, Y. Wang, A.K. Datye, Thermally stable single-atom platinum-on-ceria catalysts via atom trapping, *Science* 353 (2016) 150–154.
- [15] K. Morgan, A. Goguet, C. Hardacre, Metal redispersion strategies for recycling of supported metal catalysts: a perspective, *ACS Catal.* 5 (2015) 3430–3445.
- [16] Y. Nagai, T. Hirabayashi, K. Dohmae, N. Takagi, T. Minami, H. Shinjoh, S. Matsumoto, Sintering inhibition mechanism of platinum supported on ceria-based oxide and Pt-oxide-support interaction, *J. Catal.* 242 (2006) 103–109.
- [17] L.A. Avakyan, N.A. Kolpacheva, E.V. Paramonova, J. Singh, U. Hartfelder, J.A. van Bokhoven, L.A. Bugaev, Evolution of the atomic structure of ceria-supported platinum nanocatalysts: formation of single layer platinum oxide and Pt–O–Ce and Pt–Ce linkages, *J. Phys. Chem. C* 120 (2016) 28057–28066.
- [18] H. Deng, X. Li, Q. Peng, X. Wang, J. Chen, Y. Li, Monodisperse magnetic single-crystal ferrite microspheres, *Angew. Chem. Int. Ed. Engl.* 44 (2005) 2782–2785.
- [19] H. Chen, C. Deng, X. Zhang, Synthesis of Fe(3)O(4)@SiO(2)/PMMA core-shell magnetic microspheres for highly efficient enrichment of peptides and proteins for MALDI-ToF MS analysis, *Angew. Chem. Int. Ed. Engl.* 49 (2010) 607–611.
- [20] G. Cheng, J.L. Zhang, Y.L. Liu, D.H. Sun, J.Z. Ni, Synthesis of novel Fe₃O₄@SiO₂/CeO₂ microspheres with mesoporous shell for phosphopeptide capturing and labeling, *Chem. Commun. (Camb.)* 47 (2011) 5732–5734.
- [21] P. Lu, B.T. Qiao, N. Lu, D.C. Hyun, J.G. Wang, M.J. Kim, J.Y. Liu, Y.N. Xia, Photochemical deposition of highly dispersed Pt nanoparticles on porous CeO₂ nanofibers for the water-gas shift reaction, *Adv. Funct. Mater.* 25 (2015) 4153–4162.
- [22] C.A. Schneider, W.S. Rasband, K.W. Eliceiri, NIH Image to ImageJ: 25 years of image analysis, *Nat. Methods* 9 (2012) 671–675.
- [23] S.M. Kim, P.M. Abdala, T. Margossian, D. Hosseini, L. Foppa, A. Armutlulu, W. van Beek, A. Comas-Vives, C. Coperet, C. Muller, Cooperativity and dynamics increase the performance of NiFe dry reforming catalysts, *J. Am. Chem. Soc.* 139 (2017) 1937–1949.
- [24] P.M. Abdala, H. Mauroy, W. van Beek, A large-area CMOS detector for high-energy synchrotron powder diffraction and total scattering experiments, *J. Appl. Crystallogr.* 47 (2014) 449–457.
- [25] B. Ravel, M. Newville, ATHENA, ARTEMIS, HEPHAESTUS: data analysis for X-ray absorption spectroscopy using IFEFFIT, *J. Synchrotron Radiat.* 12 (2005) 237–241, <https://doi.org/10.1107/S0909049505012719>.
- [26] S.I. Zabinsky, J.J. Rehr, A. Ankudinov, R.C. Albers, M.J. Eller, Multiple-scattering calculations of x-ray-absorption spectra, *Phys. Rev., B Condens. Matter* 52 (1995) 2995–3009.
- [27] M. Munoz, P. Argoul, F. Farges, Continuous Cauchy wavelet transform analyses of EXAFS spectra: a qualitative approach, *Am. Mineral.* 88 (2003) 694–700.
- [28] B. McBride, M. Zehe, S. Gordon, NASA Glenn Coefficients for Calculating Thermodynamic Properties of Individual Species, NASA Report, 2002 TP-2002-211556, (2002).
- [29] S. Shaikhutdinov, H.J. Freund, Ultrathin oxide films on metal supports: structure-reactivity relations, *Annu. Rev. Phys. Chem.* 63 (2012) 619–633.
- [30] W. Liu, J.Y. Lim, M.A. Saucedo, A.N. Hayhurst, S.A. Scott, J.S. Dennis, Kinetics of the reduction of wüstite by hydrogen and carbon monoxide for the chemical looping production of hydrogen, *Chem. Eng. J.* 120 (2014) 149–166.
- [31] N.L. Galinsky, A. Shafieifarhood, Y.G. Chen, L. Neal, F.X. Li, Effect of support on redox stability of iron oxide for chemical looping conversion of methane, *Appl. Catal. B* 164 (2015) 371–379.
- [32] N.V.R.A. Dharanipragada, M. Meledina, V.V. Galvita, H. Poelman, S. Turner, G. Van Tendeloo, C. Detavernier, G.B. Marin, Deactivation study of Fe₂O₃-CeO₂ during redox cycles for CO production from CO₂, *Ind. Eng. Chem. Res.* 55 (2016) 5911–5922.
- [33] R.D. Shannon, C.T. Prewitt, Effective ionic radii in oxides and fluorides, *Acta Crystall., B-Struc.* 25 (1969) 925.
- [34] J.F. Lee, M.T. Tang, W.C. Shih, R.S. Liu, Ce K-edge EXAFS study of nanocrystalline CeO₂, *Mater. Res. Bull.* 37 (2002) 555–562.
- [35] K. Li, H. Wang, Y. Wei, D. Yan, Syngas production from methane and air via a redox process using Ce–Fe mixed oxides as oxygen carriers, *Appl. Catal. B* 97 (2010) 361–372.
- [36] M. Machida, T. Kawada, H. Fujii, S. Hinokuma, The role of CeO₂ as a gateway for oxygen storage over CeO₂-Grafted Fe₂O₃ composite materials, *J. Phys. Chem. C* 119 (2015) 24932–24941.
- [37] Y.D. Tretyakov, V.V. Sorokin, A.R. Kaul, A.P. Erastova, Phase equilibria and thermodynamics of coexisting phases in rare-earth element-iron-oxygen systems. I. The cerium-iron-oxygen system, *J. Solid State Chem.* 18 (1976) 253–261.
- [38] A.M. Ganzler, M. Casapu, P. Vernoux, S. Lorient, F.J. Cadete Santos Aires, T. Epicier, B. Betz, R. Hoyer, J.D. Grunwaldt, Tuning the structure of platinum particles on Ceria In situ for enhancing the catalytic performance of exhaust gas catalysts, *Angew. Chem. Int. Ed. Engl.* 56 (2017) 13078–13082.
- [39] S.J. Pennycook, Z-contrast stem for materials science, *Ultramicroscopy* 30 (1989) 58–69.
- [40] S.J. Pennycook, The impact of STEM aberration correction on materials science, *Ultramicroscopy* 180 (2017) 22–33.
- [41] H. Yoshida, S. Nonoyama, Y. Yazawa, T. Hattori, Quantitative determination of platinum oxidation state by XANES analysis, *Phys. Scripta T115* (2005) 813–815.